

# Ionically-Mediated Electromechanical Hysteresis in Transition Metal Oxides

Yunseok Kim,<sup>†,\*</sup> Anna N. Morozovska,<sup>‡</sup> Amit Kumar,<sup>†</sup> Stephen Jesse,<sup>†</sup> Eugene A. Eliseev,<sup>‡</sup> Fabien Alibert,<sup>§</sup> Dmitri Strukov,<sup>§</sup> and Sergei V. Kalinin<sup>†,\*</sup>

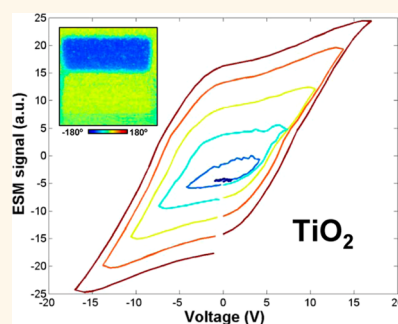
<sup>†</sup>The Center for Nanophase Materials Sciences, Oak Ridge National Laboratory, Oak Ridge, Tennessee 37831, United States, <sup>‡</sup>National Academy of Sciences of Ukraine, Kiev 03028, Ukraine, and <sup>§</sup>Department of Electrical and Computer Engineering, University of California, Santa Barbara, California 93106, United States

In the past decade, much attention has been attracted to polarization behavior in nanoscale ferroelectrics as motivated by applications ranging from ferroelectric tunneling barrier devices to domain wall conductivity.<sup>1–5</sup> In these studies, the presence of macroscopic ferroelectric domains and moving domain walls provides unambiguous evidence toward ferroelectricity. At the same time, multiple studies of polarization-mediated electroresistance or, more generally, ferroelectricity in nonclassical ferroelectric materials such as SrTiO<sub>3</sub> (STO),<sup>6–8</sup> CaCu<sub>3</sub>Ti<sub>4</sub>O<sub>12</sub>,<sup>9</sup> and manganites<sup>10</sup> report unusual polarization behavior and switching dynamics. In general, remanent polarization states, hysteresis loops, and slow relaxation of induced polarization are observed, highly reminiscent of the ferroelectric relaxors.<sup>11,12</sup> At the same time, domains and domain walls in the pristine (unpoled) state are generally not observed, consistent with nanopolar or nonferroelectric ground states.

A significant aspect of many local and device based studies of ferroelectricity and electroresistance in thin films is extremely high electric fields of the order of 10<sup>6</sup>–10<sup>7</sup> V/cm, often comparable and exceeding intrinsic coercive fields in ferroelectric materials.<sup>3</sup> In electroresistive and memristive applications of materials such as TiO<sub>2</sub> and STO,<sup>13,14</sup> the electric fields that induce nonlinear ionic drift and conductive filament formation are typically of the order of ~10<sup>7</sup> V/cm,<sup>15,16</sup> that is, comparable. Notably, electrochemistry of ferroelectric titanates such as BaTiO<sub>3</sub> can be expected to be close to that of STO and TiO<sub>2</sub>. Hence, both polarization-mediated phenomena and solid-state electrochemical ionic dynamics can potentially be involved in the bias-induced phenomena in ferroelectric thin films.

In many cases, the ferroelectric nature of material is established based on the

## ABSTRACT



Nanoscale electromechanical activity, remanent polarization states, and hysteresis loops in paraelectric TiO<sub>2</sub> and SrTiO<sub>3</sub> thin films are observed using scanning probe microscopy. The coupling between the ionic dynamics and incipient ferroelectricity in these materials is analyzed using extended Landau–Ginzburg–Devonshire (LGD) theory. The possible origins of electromechanical coupling including ionic dynamics, surface-charge induced electrostriction, and ionically induced ferroelectricity are identified. For the latter, the ionic contribution can change the sign of first order LGD expansion coefficient, rendering material effectively ferroelectric. The lifetime of these ionically induced ferroelectric states is then controlled by the transport time of the mobile ionic species and well above that of polarization switching. These studies provide possible explanation for ferroelectric-like behavior in centrosymmetric transition metal oxides.

**KEYWORDS:** electromechanical hysteresis loop · incipient ferroelectrics · ionic dynamics · transition metal oxides · ESM

presence of nanoscale electromechanical response and hysteresis loops as detected by piezoresponse force microscopy (PFM) and spectroscopy.<sup>17,18</sup> Recently, ionic hysteresis loops and strong relaxation of bias-induced electromechanical responses (albeit not domain writing), were reported in ionic conductors including Li-ion systems<sup>19</sup> and oxygen conductors such as yttrium-stabilized zirconia and Sm-doped ceria<sup>20</sup> by electrochemical strain microscopy (ESM). Here, we explore whether surface or bulk solid state ionic phenomena can explain local electromechanical responses, hysteresis

\* Address correspondence to ykim943@gmail.com, sergei2@ornl.gov.

Received for review May 10, 2012 and accepted July 30, 2012.

Published online July 30, 2012  
10.1021/nn3020757

© 2012 American Chemical Society

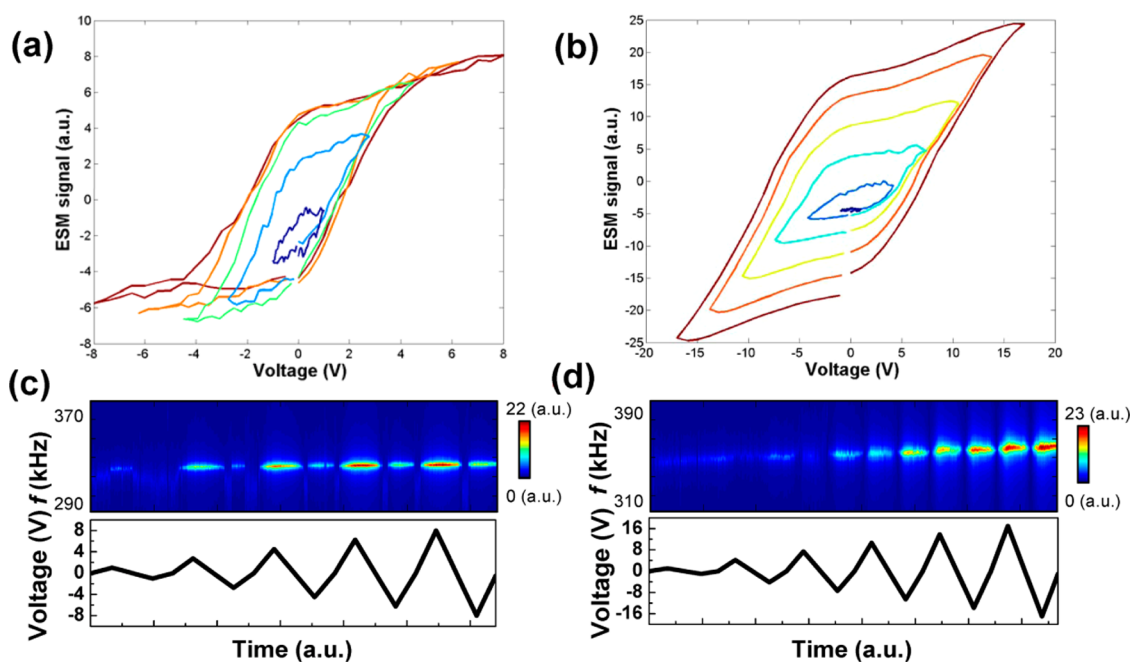


**Figure 1.** (a, b) Average FORC-type ESM loops over a spatial grid of points and (c,d) (top) single point BE amplitude spectra as a function of (bottom) varying bias voltage during the FORC acquisition in (a, c) STO and (b, d) TiO<sub>2</sub> thin films. (a, b) In both materials, clear loop opening is seen once the bias window exceeds a critical bias and (c, d) switching events are clearly observed as straight vertical lines where the amplitude of the response goes to the noise value. The pulse-type voltage sweep is performed as similar to that of Figure 2. FORC-type ESM loops are averaged from more than 100 points.

loops, and relaxor-like electromechanical behavior in oxides and establish the nature of coupling between ionic and ferroelectric behaviors.

As model systems, we have chosen STO and TiO<sub>2</sub> films. These materials have comparable electrochemical behavior (as controlled by the Ti 3d and oxygen 2p levels).<sup>21,22</sup> Furthermore, it is well established that electrochemical reactions, which can be detected by ESM,<sup>19,20</sup> play an important role on operational mechanisms in memristive behavior such as electroforming and subsequent resistive switching.<sup>13,14</sup> However, these materials have very different ferroelectric properties. While STO is incipient ferroelectric and can be transformed to ferroelectric state by compressive strain,<sup>6,7</sup> isotope substitution,<sup>23</sup> or applying electric fields,<sup>24</sup> TiO<sub>2</sub> does not have ferroelectric soft mode instability, but is an incipient ferroelectric<sup>25</sup> and is also expected to be transformed to the ferroelectric state under certain conditions.<sup>26</sup> Here, the 50 nm thick unstrained STO and 60 nm thick TiO<sub>2</sub> layers were deposited on Si/SiO<sub>2</sub> substrate by RF magnetron sputtering and atomic layer deposition, respectively. Scanning probe microscopy (SPM) studies were carried out on a commercial system (Cypher, Asylum Research) equipped with home-built Labview/Matlab based band-excitation (BE) controller for electromechanical imaging and time and voltage spectroscopies. The detailed information on the materials and methods can be found in Supporting Information.

Here, we observed that both STO and TiO<sub>2</sub> generate strong electromechanical response and exhibit

hysteresis loops for sufficiently high ( $V_{dc} > 5$  V) biases. However, single hysteresis loop is generally insufficient to fully characterize field-dependent responses and cannot distinguish bistability, kinetic, or thermodynamic Preisach-like behaviors. To explore these possibilities systematically, we employ a first order reversal curve (FORC) method.<sup>27</sup> In this, a series of hysteresis loops with increasing bias window is acquired at each location on the sample surface over  $25 \times 25$  ( $10 \times 10$ ) spatial grid of points for STO (TiO<sub>2</sub>) thin films and subsequently averaged. Shown in Figure 1a,b are FORC-type ESM hysteresis loops for STO and TiO<sub>2</sub>. Note that for both materials well-defined hysteretic responses are observed once the bias window exceeds a critical bias (2 V for both STO and TiO<sub>2</sub>). On increasing the bias, the hysteresis loops progressively open up. The nucleation biases (i.e., the inflection points on the hysteresis loops) are virtually bias-independent.

## RESULTS AND DISCUSSION

The evolution of resonance frequency during measurements can be ascertained from the voltage evolution of the BE spectra for each material, as shown in Figure 1c,d. Small but systematic increase of the resonant frequency during the measurements is indicative of the changes in mechanical properties of the tip–surface junction, for example, increase of contact area or material stiffening. Surface topography does not change in these measurements (static deformations below 1 nm). Measurements at high bias windows were limited by an onset of electronic currents

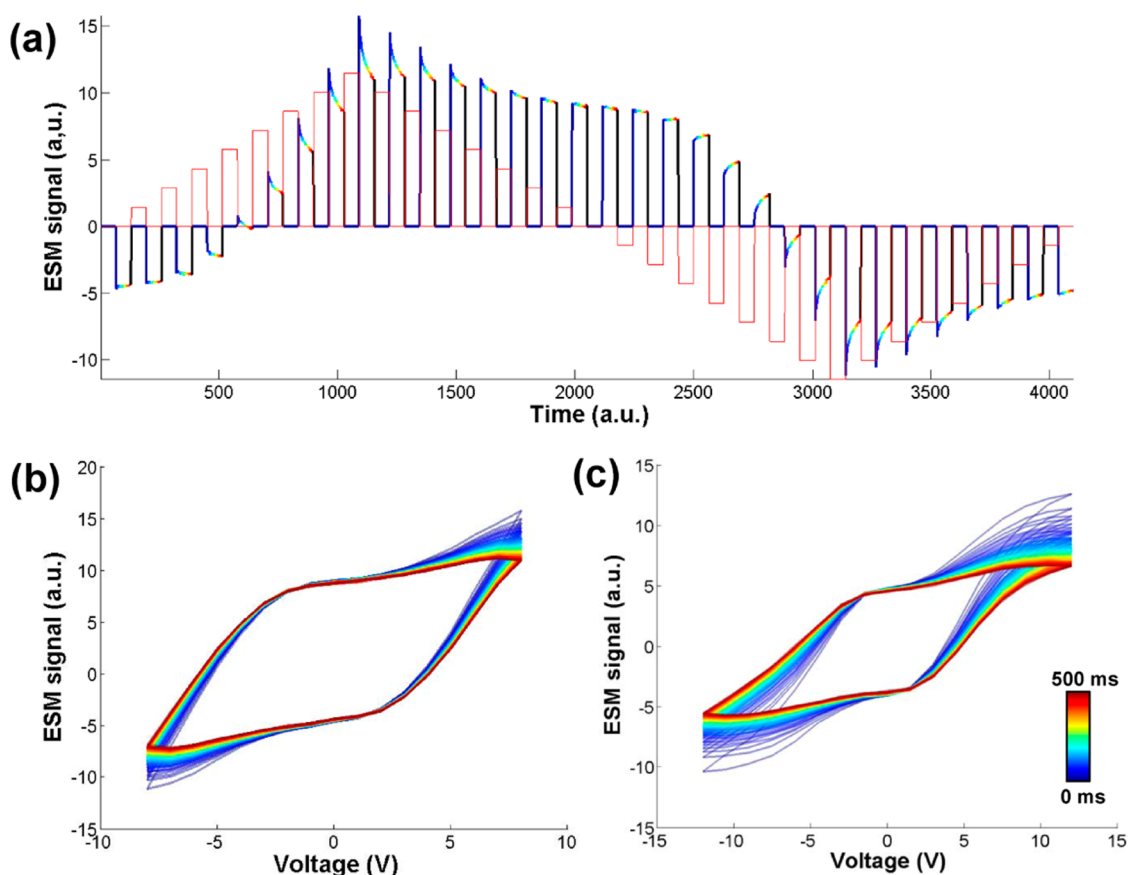


**Figure 2.** (a) Outer envelope of a triangular waveform in a D-ESM measurement overlaid on time-dependence of ESM response in STO thin films. D-ESM loops as a function of time delay illustrating relaxation dynamics for different maximum applying voltages in (b) STO and (c) TiO<sub>2</sub> thin films. D-ESM loops are averaged from more than 95 points.

and dielectric breakdown, or, under certain conditions, irreversible static deformation of the surface (electroforming).

To explore the role of time dynamics and establish presence of one or multiple thermodynamic ground states, the dynamics ESM (D-ESM) measurements were performed.<sup>28</sup> In these, the relaxation of the signal following the application of the bias pulse is measured within the loop. These data can be visualized as time-dependence of the signal, and the outer envelope of triangular bias sweep for TiO<sub>2</sub> is shown in Figure 2a, with the delay time after bias pulse marked with color. Alternatively, the dynamics can be represented as a series of time-delayed hysteresis loops, as shown in Figure 2b,c. For STO, relaxation of ESM response is relatively weak and is essentially zero within the  $\pm 2$  V window. For TiO<sub>2</sub>, the relaxation is much stronger; however, it is also nearly zero within a  $\pm 1.5$  V window. The boundaries of these no-relaxation windows are very close to the nucleation biases. These voltage regions can be interpreted as a presence of distinct thermodynamic ground states or biases corresponding to kinetic freezing of the system (nonergodic state).

To explore long-term response dynamics (i.e., presence of remanent states), a set of rectangular patterns were formed by application of biases of different

magnitudes during scanning. In both STO and TiO<sub>2</sub>, the biased patterns in the ESM phase and amplitude images resemble typical ferroelectric domain patterns. While the ESM phase of positively biased regions in both STO and TiO<sub>2</sub> is similar to the as-grown state (outside of biased region), the amplitude depends on the applying biases and is higher than the as-grown state. The negatively biased regions in both STO and TiO<sub>2</sub> thin films show distinctly higher amplitude and lower phase. The pristine surface in TiO<sub>2</sub> shows nearly zero amplitude. The switchability of induced response can further be probed by subsequent application of negative voltage within positively biased region (Supporting Information). Under higher biases, the positive and negatively biased regions are clearly visible, which shows the ferroelectric-like switching in both thin films.

These observations suggest that both STO and TiO<sub>2</sub> demonstrate remanent polarized states and hysteresis loops similar to that in ferroelectric materials. Unlike classical ferroelectrics (and similar to ergodic ferroelectric relaxors), the response in TiO<sub>2</sub> is zero outside the poled regions, that is, is voltage-activated. Partial relaxation of response, as illustrated in Figure 2, can be observed both for ferroelectric and relaxor systems. Finally, the presence of two dominant remnant

responses, well-defined nucleation biases, and lack of relaxation for the low biases are more reminiscent of classical ferroelectrics or nonergodic relaxors. However, the fact that  $\text{TiO}_2$  is a nonferroelectric material, as well as a requirement of voltage activation, precludes us from interpreting the observed behavior as purely ferroelectric or relaxor ferroelectric and strongly suggests the role of ionic and electrochemical phenomena.

Application of the electric bias to the SPM probe in contact with oxide surface and surrounded by water meniscus can give rise to a broad set of strain-coupled physical and electrochemical phenomena, including electrocapillary water condensation, water splitting, and surface charging by  $\text{H}^+$  and  $\text{OH}^-$ , vacancy motion within the material, and activation of oxygen reduction/evolution reaction of the type  $2\text{O}_2^{\times} \leftrightarrow 2\text{V}_x^{\bullet\bullet} + \text{O}_2 + 4e^-$  (likely assisted by presence of water).<sup>29,30</sup> In ferroelectrics and incipient ferroelectrics, surface charges and associated electrostatic fields can stabilize ferroelectric state.<sup>31,32</sup> Finally, more complex processes associated with reconstruction of host lattice, including vacancy segregation and formation of crystallographic shear planes or cationic demixing are possible.

Note that processes associated with lattice reconstruction will result in irreversible nonuniform changes in surface topography and are indeed observed at high ( $>+20$  V for  $\text{TiO}_2$ ) bias stresses. Here, the absence of visible topographic changes, as well as reversibility of induced responses, allows excluding these from consideration. The electrocapillary water condensation is unlikely to be the primary factor because the geometry of the tip–surface junction precludes thermodynamic (albeit not kinetic) capillary condensation hysteresis.

Of interest are the mechanisms associated with charging of surface layers. Note that formation of excess protons or hydroxyls can be readily induced by biased SPM probe. However, in the absence of bulk ionic conductance these species cannot relax through tip or surface (ionic blocking behavior) and, hence, give rise to long-lived *surface* charge states.<sup>33,34</sup> To get some insight into the process, we have performed Kelvin probe force microscopy (KPFM) studies. Here, tip-induced surface potential is measured following the poling of the surface as a function of poling bias in a manner similar to Figure 3. These studies are performed on pristine surface and surface uniformly prepoled by  $\pm 8$  V, providing analogs of KPFM hysteresis loop as shown in Figure 3c. Note, while there is a measurable hysteresis, the shape of the loop and its position is very different from the PFM loops.

These changes in surface potential as detected by KPFM are an expected effect of *bulk* charge injection.<sup>35</sup> However, *surface* charging can also provide additional contrast to PFM and ESM measurements. Specifically, it results in (a) electrostatic tip surface forces, henceforth referred to as direct surface charge effect, and (b)

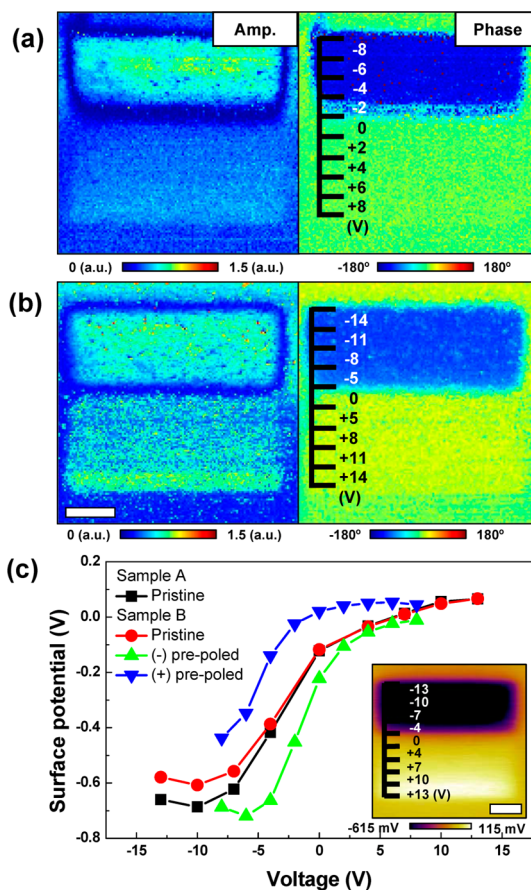


**Figure 3.** ESM amplitude and phase images of the area scanned with the applied biases from  $-8$  ( $-14$ ) to  $8$  ( $14$ ) V to the conductive probe for (a) STO [(b)  $\text{TiO}_2$ ] thin film. (c) Tip-induced surface potential as a function of poling bias on pristine surface (in  $\text{TiO}_2$  samples A and B fabricated under the same conditions) and surface uniformly prepoled by  $\pm 8$  V. Each tip-bias surface potential is averaged from each rectangular pattern. Inset of (c) shows the surface potential image of the area scanned with the applied biases from  $-13$  to  $+13$  V to the conductive probe for pristine  $\text{TiO}_2$  thin film. The scale bar is  $1.5 \mu\text{m}$ .

electrostriction of material below the tip (striction or indirect surface charge effect). Direct effect can generally be ruled out based on the comparative analysis of electrostatic and electromechanical interactions.<sup>36,37</sup> We note that, because KPFM contrast can be influenced by the measurement environment,<sup>38</sup> all SPM measurements were carried out in the same atmosphere (air).

To estimate the indirect effect, we note that surface charging will introduce a homogeneous built-in field  $E_b$  along the  $x_3$  axis that induces the piezoelectric effect. The corresponding piezoelectric coefficients are  $d_{33} = 2Q_{33}E_b/(a_3)^2$ ,  $d_{31} = 2Q_{31}E_b/(a_3)^2$ ,  $d_{15} = Q_{44}E_b/(a_3a_1)$ ,<sup>39</sup> where  $Q_{ij}$  and  $a_i$  are electrostriction strain coefficients and dielectric stiffness coefficients, respectively. The electromechanical response can then be calculated as  $(d_{31}(1 + 2\gamma)) + d_{15}\gamma^2 + d_{33}(1 + 2(1 + \gamma)\nu)/(1 + \gamma)^2$ , where  $\gamma = (\epsilon_{33}/\epsilon_{11})^{1/2}$  is the dielectric anisotropy factor and  $\nu$  is the Poisson ratio.<sup>40</sup> From measured hysteretic potential change of  $\sim 0.6$  eV, the built-in field is

estimated as  $E_b = 10^7$  V/m. Hence, the striction contribution to measured signal is estimated as  $\sim 2$  and  $\sim 3$  pm/V for  $\text{TiO}_2$  and STO, respectively. While measurable, these responses are relatively small. Indeed, a previous report on the comparison of PFM and KPFM images demonstrates that, although surface charging is drastically changed, the sign and the amount of surface charging do not significantly affect PFM phase signal.<sup>41</sup>

We further explore the coupling between ionic phenomena and incipient ferroelectric instability. To exemplify such coupling, note that injection of oxygen vacancies locally will result in the increase of lattice volume,<sup>42,43</sup> effectively resulting in compressive strain on the biased region. To describe this behavior, we consider the Landau–Ginzburg free energy for incipient ferroelectric as  $F_b = F_f + F_s + F_{ec}$ .<sup>25</sup> Here,  $F_f$  is the classical ferroelectric Landau–Ginzburg–Devonshire (LGD) term:

$$F_f = \frac{a_i(T)}{2} P_i^2 + \frac{a_{ij}}{4} P_i^2 P_j^2 + \dots - P_i \left( \frac{E_i^d}{2} + E_i^{\text{ext}} \right) + q_{ijkl} u_{ij} P_k P_l + \frac{f_{ijkl}}{2} \left( \frac{\partial P_k}{\partial x_l} u_{ij} - P_k \frac{\partial u_{ij}}{\partial x_l} \right) \quad (1)$$

where  $P_k$ ,  $u_{ij}(\mathbf{x})$ ,  $E_i$ ,  $f_{ijkl}$ ,  $q_{ijkl}$ ,  $c_{ijkl}$ , and  $a_i(T)$  are polarization vector components, strain tensor, electric field, tensor of flexoelectric coupling, electrostriction stress tensor, elastic stiffness, and expansion coefficient, respectively. The expansion coefficient  $a_i(T) > 0$  depends on temperature in accordance with Barrett law  $a_i(T) = \alpha_{Ti}(\coth(T_q/(2T))T_q/2 - T_0)$ .<sup>29,44</sup> In addition, strain energy and electrochemical contribution are  $F_s = ((c_{ijkl})/(2))u_{ij}u_{kl}$  and  $F_{ec} = \Xi_{ij}^C u_{ij}(n - n_e) + \beta_{ij}^d u_{ij}(N_d^+ - N_{de}^+)$ , respectively. In the latter, the first term is due to the deformation potential,  $\Xi_{ij}^C$ , and  $(n - n_e)$  is excess carrier concentration. The second is the chemical expansion term,  $\beta_{ij}^d$  is Vegard expansion tensor, and  $(N_d^+ - N_{de}^+)$  is excess ionic concentration.<sup>29</sup>

Polarization  $P_k$  can then be determined from the LGD-type equations  $\partial F_b / \partial P_k = 0$  leading to  $\alpha_i^R(T, \varphi) P_i + a_{ik} P_k^2 P_i - g \Delta P_k = -\partial \varphi / \partial x_i$ . This analysis yields that the coefficient  $\alpha_i^R(T, \varphi)$  depends on the concentration of electrons and vacancies as

$$\alpha_i^R(T, \varphi) \approx a_i(T) + 2Q_{ijkl}(\Xi_{ij}^C(n - n_e) + \beta_{ij}^d(N_d^+ - N_{de}^+)) \quad (2)$$

Notably, eq 2 suggests that vacancy injection can change alpha  $\alpha_i^R$  and in particular change its sign (i.e.,  $\alpha_i^R < 0$ ), that is, induce ferroelectric instability in the material.

Using material parameters for STO and  $\text{TiO}_2$  (Table 1 of Supporting Information), we estimate that the redistribution of electrons (in the effective mass approximation<sup>45,46</sup>) cannot lead to the negative  $\alpha_i^R(T, \varphi)$  at room temperature and applied bias range  $|V| \sim 1$ –10 V. At the same time, vacancy redistribution can lead to the negative alpha at biases  $> 1$  V at  $N_{do}^+ \sim 10^{20} \text{ m}^{-3}$  and high  $N_{\text{max}} \sim 10^{27} \text{ m}^{-3}$  (see Figure 4c). While the lateral extent is determined by the tip size

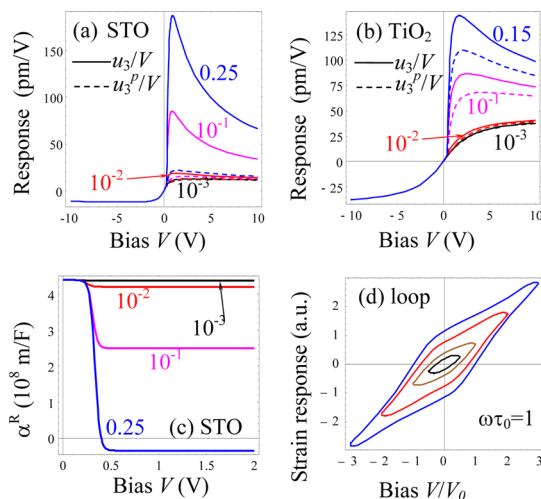


**Figure 4.** Static polarization-dependent  $u_3^p(0)/V$  (dashed curves) and total  $u_3(0)/V$  (solid curves) strain responses vs applied bias  $V$  calculated for (a) STO and (b)  $\text{TiO}_2$  material parameters. Different curves correspond to different values of donor maximal concentration  $N_{\text{max}}/N_0 = 10^{-3}$ ,  $10^{-2}$ ,  $10^{-1}$ , 0.25 (figures near the curves), where  $N_0 = 1/(4A)^3$  is the physical limit (“concentration” of unit cells of STO);  $\beta_{33}^d = 20 \text{ eV}$ ,  $N_{do}^+ = 10^{20} \text{ m}^{-3}$ . (c) Renormalized coefficient  $\alpha^R$  vs tip bias at distance  $z = 0$ . Other material parameters are listed in Table 1 of the Supporting Information. (d) Dynamic strain–voltage response loops calculated for different bias windows.

$R_0 \sim 10$ –100 nm, the penetration depth of this local polar state increases with increasing applied voltage.

The surface vertical displacement, measured by SPM, is<sup>33</sup>

$$u_3(0) = \int_h^0 (u_{33}^{\text{ion}}(z') + u_{33}^p(z')) dz' \quad (3)$$

where the ionic contribution is  $u_{33}^{\text{ion}}(z') = -s_{33ij}(\Xi_{ij}^C(n - n_e) + \beta_{ij}^d(N_d^+ - N_{de}^+))$  and the contribution of flexoelectric and electrostrictive effects is  $u_{33}^p(z') = -s_{33ij} (f_{ijmn}(\partial P_n / \partial x_m) + q_{ijmn} P_m P_n)$ . Static total  $u_3$  (solid curves) and polarization-dependent  $u_3^p$  (dashed curves) responses are shown in Figure 4a,b. Note that ionic and induced polarization contributions are comparable for  $\text{TiO}_2$ , while the ionic response dominates for STO. In comparison, the striction effect is significantly smaller.

To calculate the dynamic response, we assume that the ionic dynamics in rigid dielectric material is controlled by a single relaxation time, for example, diffusion time of the ion on the length scale of tip radius. In the presence of dielectric nonlinearity, the relaxation time is normalized as (see Supporting Information)

$$\tau(V) = \tau_0 \frac{\varepsilon(V)}{\varepsilon(0)} \sim \frac{\tau_0}{1 + (V/V_0)^2} \quad (4)$$

where  $V_0 = R_0 E_c$  is determined by the characteristic field  $E_c = (4|a_1^3|/27a_{11})^{1/2}$  ( $R_0$  is the characteristic tip size). The nonlinear response can then be calculated using the Fourier transform of the triangular bias pulse as  $u_3(t) = \text{Re}[\sum_{n=1}^{\infty} Z(n\omega) V_n \exp(in\omega t)]$ , where  $V_n = 4V_{in}/\pi^2 n^2 \sin^2(\pi n/2)$  and  $Z(\omega) = (1 + i\omega\tau(V))^{-1}$ . Strain

response loops for different bias windows are shown in Figure 4d. At a small bias window the loops are elliptic (linear response) and adopt a quasi-rhombic shape for higher bias windows. The evolution of the loop shape is similar to the experimental ones shown in Figure 1b. We note that the lifetimes of injected vacancies can be quite large for realistic materials and exceed by many orders of magnitude time scales required for, for example, polarization switching. Hence, this state can be understood as a ferroelectric state as long as vacancies persist. However, we specifically note that this phenomenon in  $\text{TiO}_2$  is different from incipient ferroelectricity, which can be transformed by, for example, chemical modification and mechanical stress, previously observed in STO.

In the last several years, much attention was attracted to the possible role of flexoelectric coupling in nanoscale systems including 2D materials,<sup>47,48</sup> biological materials,<sup>49</sup> and ferroelectrics.<sup>50,51</sup> We further note that “pure” flexoelectric effect cannot induce the thermodynamically stable hysteresis loop in incipient ferroelectrics (or quantum paraelectrics) such as STO<sup>30</sup> and materials such as  $\text{TiO}_2$ . However, the vertical dc offset of the loop is quite possible in the materials with strong flexoelectric coupling and strongly inhomogeneous strains/stress fields. In particular, the difference of current results with those obtained in STO ceramics can be explained by the different manifestation of flexoelectric coupling in the materials,<sup>8</sup> because elastic field strength and inhomogeneity are extremely sensitive to the mechanical clamping (e.g., substrate/bottom electrode impact) and extended elastic defects (e.g., intergrain space structure, clusters, dislocations, etc.).

We further note that relatively complex kinetic (relaxation) behavior of the local piezoresponse in

Figure 2 can be attributed with oxygen vacancies or other mobile species redistribution induced by electric field. Because the two-stage relaxation was observed and also attributed to the oxygen vacancy redistribution under applied electric field in relaxor ferroelectric  $\text{PbMn}_{1/3}\text{Nb}_{2/3}\text{O}_3$  thin films,<sup>52</sup> piezoresponse relaxation originated from the vacancies redistribution may have universal features in relaxors, incipient ferroelectrics, and even in rutile.

## SUMMARY

To summarize, electromechanical response, hysteresis, relaxation, and remanent states were observed in STO and  $\text{TiO}_2$  thin films. While significantly different in terms of ferroelectric behavior, these materials have very similar solid state electrochemical behavior. Based on the experimental observations, we ascribe electromechanical responses to bulk ionic processes. Theoretical results indicate the coupling between ionic processes and incipient ferroelectric instability will give rise to hysteric behavior in these materials.

These conclusions can open a new perspective on recent studies of polarization-mediated tunneling in ultrathin ferroelectrics. Note that while electromechanical response is possible even in the absence of ferroelectricity, these studies do not exclude presence of ferroelectricity, given that charge-specific adsorption that stabilizes ferroelectric state.<sup>53</sup> These studies furthermore illustrate that piezoresponse and electrochemical strain microscopy and spectroscopy can be a powerful tool for probing memristive behavior at early stages, providing information on ionic dynamics preceding the electroforming<sup>13,14</sup> as well as studying  $\text{LaAlO}_3/\text{STO}$  and other systems, where ions can be involved.<sup>54–56</sup>

## METHODS

**Materials.** The 50 nm thick unstrained STO and 60 nm thick  $\text{TiO}_2$  amorphous layers were both deposited on  $\text{Si}/\text{SiO}_2$  substrate with patterned bottom electrodes (BE). The  $\text{Ti}(5 \text{ nm})/\text{Pt}(25 \text{ nm})$  BE were patterned by conventional photolithography. Before the e-beam evaporation of the metal layers, a descum cleaning step ( $\text{O}_2$  plasma during 30 s) was realized to remove any organic layer from the  $\text{SiO}_2$  surface. The STO thin film was then deposited by RF magnetron sputtering of a STO target in  $\text{Ar}/\text{O}_2$  plasma (80/20 ratio) at  $T = 800 \text{ }^\circ\text{C}$ , while the  $\text{TiO}_2$  layer was realized by atomic layer deposition at  $200 \text{ }^\circ\text{C}$  using titanium isopropoxide ( $\text{C}_{12}\text{H}_{28}\text{O}_4\text{Ti}$ ) and water as a precursor and reactant, respectively. Finally, the BE was accessed by local etching of the STO and  $\text{TiO}_2$  by dry etching process using  $\text{CHF}_3$  plasma.

**Measurements.** Scanning probe microscopy (SPM) studies were carried out on a commercial system (Asylum Cypher) equipped with home-built Labview/Matlab based band-excitation (BE) controller.<sup>57</sup> Excitation was performed using BE waveform of 80–100 kHz width centered on the first contact resonance (300–425 kHz) and amplitude of  $1.5 V_{\text{pp}}$  applied directly to a Pt/Cr-coated probe (Budget sensors ElectriMulti75-G). The hysteresis loop measurements are performed in the off-field mode, that is, following the application of bias pulse of

given amplitude. For Kelvin probe force microscopy (KPFM) measurements, first trace was carried out on noncontact mode for recording topographic information, and then a second trace was performed with an application of  $0.6 V_{\text{pp}}$  and 50 nm lift-off height for recording surface potential. Each rectangular area was scanned with the applied biases from  $-13$  to  $+13 \text{ V}$  to the conductive probe for the pristine surface and surface prepoled by  $\pm 8 \text{ V}$  of  $\text{TiO}_2$  thin films. Each tip-bias surface potential is averaged from each rectangular pattern. All of SPM measurements were carried out in air.

*Conflict of Interest:* The authors declare no competing financial interest.

*Acknowledgment.* This research was supported (S.V.K., Y.K.) by the U.S. Department of Energy, Basic Energy Sciences, Materials Sciences and Engineering Division. The SPM techniques were developed at the Center for Nanophase Materials Sciences (S.J.), which is sponsored at Oak Ridge National Laboratory by the Office of Basic Energy Sciences, U.S. Department of Energy. UCSB is partially funded by Air Force Office of Scientific Research under Contract No. FA9550-10-C-0083.

*Supporting Information Available:* D-ESM spectra, ESM images of biased square patterns, and equations and figures for ferroelectric-like piezoresponse induced by mobile ions in

incipient ferroelectrics. This material is available free of charge via the Internet at <http://pubs.acs.org>.

## REFERENCES AND NOTES

- Kohlstedt, R.; Pertsev, R. A.; Rodríguez Contreras, J.; Waser, R. Theoretical Current-Voltage Characteristics of Ferroelectric Tunnel Junctions. *Phys. Rev. B* **2005**, *72*, 125341.
- Maksymovych, P.; Jesse, S.; Yu, P.; Ramesh, R.; Baddorf, A. P.; Kalinin, S. V. Polarization Control of Electron Tunneling into Ferroelectric Surfaces. *Science* **2009**, *324*, 1421–1425.
- García, V.; Fusil, S.; Bouzehouane, K.; Enouz-Vedrenne, S.; Mathur, N. D.; Barthelemy, A.; Bibes, M. Giant Tunnel Electroresistance for Non-Destructive Readout of Ferroelectric States. *Nature* **2009**, *460*, 81–84.
- Pantel, D.; Goetze, S.; Hesse, D.; Alexe, M. Room-Temperature Ferroelectric Resistive Switching in Ultrathin Pb-(Zr<sub>0.2</sub>Ti<sub>0.8</sub>)O<sub>3</sub> Films. *ACS Nano* **2011**, *5*, 6032–6038.
- Seidel, J.; Martin, L. W.; He, Q.; Zhan, Q.; Chu, Y.-H.; Rother, A.; Hawkrige, M. E.; Maksymovych, P.; Yu, P.; Gajek, M.; Balke, N.; Kalinin, S. V.; Gemming, S.; Wang, F.; Catalan, G.; Scott, J. F.; Spaldin, N. A.; Orenstein, J.; Ramesh, R. Conduction at Domain Walls in Oxide Multiferroics. *Nat. Mater.* **2009**, *8*, 229–234.
- Haeni, J. H.; Irvin, P.; Chang, W.; Uecker, R.; Reiche, P.; Li, Y. L.; Choudhury, S.; Tian, W.; Hawley, M. E.; Craigo, B.; Tagantsev, A. K.; Pan, X. Q.; Streiffer, S. K.; Chen, L. Q.; Kirchoefer, S. W.; Levy, J.; Schlom, D. G. Room-Temperature Ferroelectricity in Strained SrTiO<sub>3</sub>. *Nature* **2004**, *430*, 758.
- Warusawithana, M. P.; Cen, C.; Sleasman, C. R.; Woicik, J. C.; Li, Y.; Kourkoutis, L. F.; Klug, J. A.; Li, H.; Ryan, P.; Wang, L.-P.; Bedzyk, M.; Muller, D. A.; Chen, L.-Q.; Levy, J.; Schlom, D. G. A Ferroelectric Oxide Made Directly on Silicon. *Science* **2009**, *324*, 367.
- Kholkin, A.; Bdikin, I.; Ostapchuk, T.; Petzelt, J. Room Temperature Surface Piezoelectricity in SrTiO<sub>3</sub> Ceramics via Piezoresponse Force Microscopy. *Appl. Phys. Lett.* **2008**, *93*, 222905.
- Tararam, R.; Bdikin, I.; Panwar, N.; Varela, J. A.; Bueno, P. R.; Kholkin, A. Nanoscale Electromechanical Properties of CaCu<sub>3</sub>Ti<sub>4</sub>O<sub>12</sub> Ceramics. *J. Appl. Phys.* **2011**, *110*, 052019.
- Mamin, R. F.; Bdikin, I. K.; Kholkin, A. L. Locally Induced Charged States in La<sub>0.89</sub>Sr<sub>0.11</sub>MnO<sub>3</sub> Single Crystals. *Appl. Phys. Lett.* **2009**, *94*, 222901.
- Shvartsman, V. V.; Kholkin, A. L. Domain Structure of 0.8Pb(Mg<sub>1/3</sub>Nb<sub>2/3</sub>)O<sub>3</sub>-0.2PbTiO<sub>3</sub> Studied by Piezoresponse Force Microscopy. *Phys. Rev. B* **2004**, *69*, 014102.
- Viehland, D.; Li, J. F.; Jang, S. J.; Cross, L. E.; Wuttig, M. Glassy Polarization Behavior of Relaxor Ferroelectrics. *Phys. Rev. B* **1992**, *46*, 8013–8017.
- Strukov, D. B.; Snider, G. S.; Stewart, D. R.; Williams, R. S. The Missing Memristor Found. *Nature* **2008**, *453*, 80–83.
- Szot, K.; Speier, W.; Bihlmayer, G.; Waser, R. Switching the Electrical Resistance of Individual Dislocations in Single-Crystalline SrTiO<sub>3</sub>. *Nat. Mater.* **2006**, *5*, 312.
- Strukov, D. B.; Williams, R. S. Exponential Ionic Drift: Fast Switching and Low Volatility of Thin-Film Memristors. *Appl. Phys. A: Mater. Sci. Process.* **2009**, *94*, 515–519.
- Noman, M.; Jiang, W.; Salvador, P. A.; Skowronski, M.; Bain, J. A. Computational Investigations into the Operating Window for Memristive Devices based on Homogeneous Ionic Motion. *Appl. Phys. A: Mater. Sci. Process.* **2011**, *102*, 877–883.
- Gruverman, A.; Kholkin, A. Nanoscale Ferroelectrics: Processing, Characterization and Future Trends. *Rep. Prog. Phys.* **2006**, *69*, 2443–2472.
- Kalinin, S. V.; Morozovska, A. N.; Chen, L. Q.; Rodriguez, B. J. Real-Space Mapping of Dynamic Phenomena During Hysteresis Loop. *Rep. Prog. Phys.* **2010**, *73*, 056502.
- Balke, N.; Jesse, S.; Morozovska, A. N.; Eliseev, E.; Chung, D. W.; Kim, Y.; Adamczyk, L.; García, R. E.; Dudney, N.; Kalinin, S. V. Nanoscale Mapping of Ion Diffusion in a Lithium-Ion Battery Cathode. *Nat. Nanotechnol.* **2010**, *5*, 749.
- Kumar, A.; Ciucci, F.; Morozovska, A. N.; Kalinin, S. V.; Jesse, S. Measuring Oxygen Reduction/Evolution Reactions on the Nanoscale. *Nat. Chem.* **2011**, *3*, 707.
- Tanaka, T.; Matsunaga, K.; Ikuhara, Y.; Yamamoto, T. First-Principles Study on Structures and Energetics of Intrinsic Vacancies in SrTiO<sub>3</sub>. *Phys. Rev. B* **2003**, *68*, 205213.
- Park, S.-G.; Magyari-Köpe, B.; Nishi, Y. Electronic Correlation Effects in Reduced Rutile TiO<sub>2</sub> within the LDA+U Method. *Phys. Rev. B* **2010**, *82*, 115109.
- Venturini, E. L.; Samara, G. A.; Itoh, M.; Wang, R. Pressure as a Probe of the Physics of <sup>18</sup>O-Substituted SrTiO<sub>3</sub>. *Phys. Rev. B* **2004**, *69*, 184105.
- Fleury, P. A.; Worlock, J. M. Electric-Field-Induced Raman Scattering in SrTiO<sub>3</sub> and KTaO<sub>3</sub>. *Phys. Rev.* **1968**, *174*, 613–623.
- Samara, G. A.; Peercy, P. S. Pressure and Temperature Dependence of the Static Dielectric Constants and Raman Spectra of TiO<sub>2</sub>. *Phys. Rev. B* **1973**, *7*, 1131.
- Grünebohm, A.; Ederer, C.; Entel, P. First-Principles Study of the Influence of (110)-Oriented Strain on the Ferroelectric Properties of Rutile TiO<sub>2</sub>. *Phys. Rev. B* **2011**, *84*, 132105.
- Mayergoyz, I. D. *Mathematical Models Of Hysteresis*; Springer: New York, 1990.
- Kumar, A.; Ovchinnikov, O. S.; Funakubo, H.; Jesse, S.; Kalinin, S. V. Real-Space Mapping of Dynamic Phenomena During Hysteresis Loop Measurements: Dynamic Switching Spectroscopy Piezoresponse Force Microscopy. *Appl. Phys. Lett.* **2011**, *98*, 202903.
- Morozovska, A. N.; Svechnikov, S. V.; Eliseev, E. A.; Jesse, E.; Rodriguez, B. J.; Kalinin, S. V. The Piezoresponse Force Microscopy of Surface Layers and Thin Films: Effective Response and Resolution Function. *J. Appl. Phys.* **2007**, *102*, 114108.
- Morozovska, A. N.; Eliseev, E. A.; Svechnikov, G. S.; Kalinin, S. V. Nanoscale Electromechanics of Paraelectric Materials with Mobile Charges: Size Effects and Nonlinearity of Electromechanical Response of SrTiO<sub>3</sub> Films. *Phys. Rev. B* **2011**, *84*, 045402.
- Highland, M. J.; Fister, T. T.; Richard, M.-I.; Fong, D. D.; Fuoss, P. H.; Thompson, C.; Eastman, J. A.; Streiffer, S. K.; Stephenson, G. B. Polarization Switching without Domain Formation at the Intrinsic Coercive Field in Ultrathin Ferroelectric PbTiO<sub>3</sub>. *Phys. Rev. Lett.* **2010**, *105*, 167601.
- Highland, M. J.; Fister, T. T.; Fong, D. D.; Fuoss, P. H.; Thompson, C.; Eastman, J. A.; Streiffer, S. K.; Stephenson, G. B. Equilibrium Polarization of Ultrathin PbTiO<sub>3</sub> with Surface Compensation Controlled by Oxygen Partial Pressure. *Phys. Rev. Lett.* **2011**, *107*, 187602.
- Kalinin, S. V.; Bonnell, D. A. Screening Phenomena on Oxide Surfaces and Its Implications for Local Electrostatic and Transport Measurements. *Nano Lett.* **2004**, *4*, 555–560.
- Kalinin, S. V.; Shin, J.; Jesse, S.; Geohegan, D.; Baddorf, A. P.; Lilach, Y.; Moskovits, M.; Kolmakov, A. Electronic Transport Imaging in a Multiwire SnO<sub>2</sub> Chemical Field-Effect Transistor Device. *J. Appl. Phys.* **2005**, *98*, 044503.
- Schirmeisen, A.; Taskiran, A.; Fuchs, H.; Bracht, H.; Murugavel, S.; Roling, B. Fast Interfacial Ionic Conduction in Nanostructured Glass Ceramics. *Phys. Rev. Lett.* **2007**, *98*, 225901.
- Kalinin, S. V.; Karapetian, E.; Kachanov, M. Nanoelectromechanics of Piezoresponse Force Microscopy. *Phys. Rev. B* **2004**, *70*, 184101.
- Kalinin, S. V.; Bonnell, D. A. Imaging Mechanism of Piezoresponse Force Microscopy of Ferroelectric Surfaces. *Phys. Rev. B* **2002**, *65*, 125408.
- Kim, H.; Hong, S.; Kim, D.-W. Ambient Effects on Electric-Field-Induced Local Change Modification of TiO<sub>2</sub>. *Appl. Phys. Lett.* **2012**, *100*, 022901.
- Cross, L. E. Ferroelectric Ceramics: Tailoring Properties for Specific Application. In *Ferroelectric Ceramics*; Setter, N., Colla, E. L., Eds.; Birkhauser Verlag: Basel, 1993; pp 1–85.
- Eliseev, E. A.; Kalinin, S. V.; Jesse, S.; Bravina, S. L.; Morozovska, A. N. Electromechanical Detection in Scanning Probe Microscopy: Tip Models and Materials Contrast. *J. Appl. Phys.* **2007**, *102*, 014109.
- Kim, Y.; Bae, C.; Ryu, K.; Ko, H.; Kim, Y. K.; Hong, S.; Shin, H. Origin of Surface Potential Change during Ferroelectric

- Switching in Epitaxial PbTiO<sub>3</sub> Thin Films Studied by Scanning Probe Microscopy. *Appl. Phys. Lett.* **2009**, *94*, 032907.
42. Gong, W.; Yun, H.; Ning, Y. B.; Greedan, J. E.; Datars, W. R.; Stager, C. V. Oxygen-Deficient SrTiO<sub>3-x</sub>,  $x = 0.28, 0.17,$  and  $0.08$ . Crystal Growth, Crystal Structure, Magnetic, and Transport Properties. *J. Solid State Chem.* **1991**, *90*, 320.
  43. Kim, Y. S.; Kim, D. J.; Kim, T. H.; Noh, T. W.; Choi, J. S.; Park, B. H.; Yoon, J.-G. Observation of Room-Temperature Ferroelectricity in Tetragonal Strontium Titanate Thin Films on SrTiO<sub>3</sub>(001) Substrates. *Appl. Phys. Lett.* **2007**, *91*, 042908.
  44. Rupprecht, G.; Bell, R. O. Dielectric Constant in Paraelectric Perovskites. *Phys. Rev.* **1964**, *135*, A748.
  45. Morozovska, A. N.; Eliseev, E. A.; Tagantsev, A. K.; Bravina, S. L.; Chen, L.-Q.; Kalinin, S. V. Thermodynamics of Electro-mechanically Coupled Mixed Ionic-Electronic Conductors: Deformation Potential, Vegard Strains, and Flexoelectric Effect. *Phys. Rev. B* **2011**, *83*, 195313.
  46. Eliseev, E. A.; Morozovska, A. N.; Svechnikov, G. S.; Gopalan, V.; Shur, V. Ya. Static Conductivity of Charged Domain Walls in uniaxial Ferroelectric Semiconductors. *Phys. Rev. B* **2011**, *83*, 235313.
  47. Kalinin, S.; Menuier, V. Electronic Flexoelectricity in Low-Dimensional Systems. *Phys. Rev. B* **2008**, *77*, 033403.
  48. Tagantsev, A. K.; Meunier, V.; Sharma, P. Novel Electro-mechanical Phenomena at the Nanoscale: Phenomenological Theory and Atomistic Modeling. *MRS Bull.* **2009**, *34*, 643–547.
  49. Kalinin, S. V.; Jesse, S.; Liu, W.; Balandin, A. A. Evidence for Possible Flexoelectricity in Tobacco Mosaic Viruses Used as Nanotemplates. *Appl. Phys. Lett.* **2006**, *88*, 153902.
  50. Catalan, G.; Lubk, A.; Vlooswijk, A. H. G.; Snoeck, E.; Magen, C.; Janssens, A.; Rispens, G.; Rijnders, G.; Blank, D. H. A.; Noheda, B. Flexoelectric Rotation of Polarization in Ferroelectric Thin Films. *Nat. Mater.* **2011**, *10*, 963–967.
  51. Lu, H.; Bark, C.-W.; Esque de los Ojos, D.; Alcalá, J.; Eom, C. B.; Catalan, G.; Gruverman, A. Mechanical Writing of Ferroelectric Polarization. *Science* **2012**, *336*, 59–61.
  52. Shvartsman, V. V.; Kholkin, A. L.; Tyunina, M.; Levoska, J. Relaxation of Induced Polar State in Relaxer PbMg<sub>1/3</sub>Nb<sub>2/3</sub>O<sub>3</sub> Thin Films Studied by Piezoresponse Force Microscopy. *Appl. Phys. Lett.* **2005**, *86*, 222907.
  53. Fong, D. D.; Kolpak, A. M.; Eastman, J. A.; Streiffer, S. K.; Fuoss, P. H.; Stephenson, G. B.; Kim, D. M.; Choi, K. J.; Eom, C. B.; Grinberg, I.; Rappe, A. M. Stabilization of Monodomain Polarization in Ultrathin PbTiO<sub>3</sub> Films. *Phys. Rev. Lett.* **2006**, *96*, 127601.
  54. Ohtomo, A.; Hwang, H. Y. A High-Mobility Electron Gas at the LaAlO<sub>3</sub>/SrTiO<sub>3</sub> Heterointerface. *Nature* **2004**, *427*, 423.
  55. Bark, C. W.; Sharma, P.; Wang, Y.; Baek, S. H.; Lee, S.; Ryu, S.; Folkman, C. M.; Paudel, T. R.; Kumar, A.; Sokolov, A.; Tsybal, E. Y.; Rzchowski, M. S.; Gruverman, A.; Eom, C. B. Switchable Induced Polarization in LaAlO<sub>3</sub>/SrTiO<sub>3</sub> Heterostructures. *Nano Lett.* **2012**, *12*, 1765–1771.
  56. Kumar, A.; Arruda, M. T.; Kim, Y.; Ivanov, I. N.; Jesse, S.; Bark, C. W.; Bristowe, N. C.; Artacho, E.; Littlewood, P. B.; Eom, C.-B.; Kalinin, S. V. Probing Surface and Bulk Electrochemical Processes on the LaAlO<sub>3</sub>/SrTiO<sub>3</sub> Interface. *ACS Nano* **2012** ASAP.
  57. Jesse, S.; Maksymovych, P.; Kalinin, S. V. Rapid Multidimensional Data Acquisition in Scanning Probe Microscopy Applied to Local Polarization Dynamics and Voltage Dependent Contact Mechanics. *Appl. Phys. Lett.* **2008**, *93*, 112903.